Effects of spatial resolution of digital terrain obtained by drone on mountainous urban fluvial flood modeling

Xingyu Zhou [1, 2], Lunwu Mou [3], Tianqi Ao[1, 2], Xiaorong Huang [1, 2], Haiyan Yang [3,4]

[1] State Key Laboratory of Hydraulics and Mountain River Engineering, Sichuan University, Chengdu 610065, China

[2] College of Water Resource & Hydropower, Sichuan University, Chengdu 610065, China

[3] Sichuan Dazhou Hydrological and Water Resources Survey Centre, Dazhou 635000, China

[4] School of Water Conservancy, North China University of Water Resources and Electric Power, Zhengzhou 450046, China

Correspondence to: Xiaorong Huang (hxiaorong@scu.edu.cn)

Abstract: The effect of resolution and quality of terrain data, as the most sensitive input to 2D hydrodynamic modeling, has been one of the main research areas in flood modeling. However, previous studies have lacked discussion on the limitations of the target area and the data source, as well as the underlying causes of simulation bias due to different resolutions. This study first discusses the performance of high-resolution Digital Terrain Model (DTM) acquired by drone for flood modeling in a mountainous riverine city, and the effect of DTM resolution on results using grid resolutions from 6 cm to 30 m. The study then investigates the root causes of the effect based on topographic attributes. Xuanhan City, a riverine city in the mountainous region of southwest China, was used as the study area. The HEC-RAS 2D model was used for all simulations, and the results generated using 6 cm DTM acquired by drone were used as a benchmark. The results indicate that flood characteristic simulations exhibit noticeable stepwise changes as DTM resolution varies. DTMs with a resolution better than 10 meters are more effective in capturing the terrain's undulating features in the study area, which is crucial for accurately modeling the inundation area. However, to accurately capture topographic features related to elevation differences, the resolution should preferably be better than 5 m, as this directly affects the accuracy of flood depth simulation. The analysis of topographic attributes provides theoretical support for determining the optimal resolution to meet simulation requirements.

Keywords: Drone, digital surface model, spatial resolution, urban fluvial flood modeling, mountainous topographic attributes

1 Introduction

Over the past decade, floods, storms and droughts together have caused 80%-90% of the worldwide natural disasters, with floods alone accounting for over 40% (WHO,2020). More than 2 billion people worldwide have been impacted by flood events, with flood-related fatalities comprising half of the total deaths from natural disasters (Alderman et al., 2012;Samela et al., 2016). With the continuous development of residential areas on the floodplains and the increasing frequency of extreme

29 precipitation events caused by the El Niño phenomenon, nearly 40% of the global cities will be located in flood-prone areas
30 by 2030, especially the mountainous cities along the rivers (Güneralp et al., 2015; Corringham and Cayan, 2019; Muthusamy
31 et al., 2021).
32
33 Taking the southwest mountainous area of China as an example, the expansion of numerous towns along major rivers in recent
34 decades has been influenced by complex topography and steep terrain. Different from the urban waterlogging caused by the
35 impermeable surface and drainage network in the plain cities, mountainous cities along rivers face distinct challenges. On the
36 one hand, the steep terrain accelerates the process of runoff entering rivers during heavy rainfall events. On the other hand,
37 early urban development in these areas was constrained by limited financial resources and inadequate planning foresight,
38 resulting in substandard river flood control infrastructure and poorly planned residential zones. Consequently, these areas are
39 more susceptible to inundation caused by the rapid rise and fall of river floods. With the growing impacts of climate change
40 and extreme weather events, flood inundation in these regions is expected to cause far greater damage than previously
41 anticipated (Xing et al., 2018; Utlu and Özdemir, 2021). Therefore, identifying potential flood-prone areas in mountainous
42 cities along rivers is critical for flood risk assessment and future urban planning. Hydrodynamic flood modeling methods are
43 indispensable for flood inundation simulation and risk management, and various GIS-based hydrodynamic flood models have
44 been developed in recent years (Azizian and Brocca, 2020; Utlu and Özdemir, 2021).
45
46 Utilizing hydrodynamic models for flood risk assessment and management necessitates a variety of data inputs, including
47 topographic and hydrological data. Over the past decade, advancements in satellite remote sensing technology and
48 computational capacity have facilitated the broader application of 2D hydrodynamic models for flood simulations (Bates, 2012;
49 Yan et al., 2015; Utlu and Ozdemir, 2020). The most sensitive input affecting the 2D flood inundation simulation attributes
50 (depth, extent, velocity) is the digital elevation model (DEM), which places higher requirements on the quality and resolution
51 of the DEM (Cook and Merwade, 2009; da Costa et al., 2019). Currently, tfreely available global DEM datasets are primarily
52 sourced from satellite imagery and include options such as the SRTM DEM (30 – 90 m), ASTER GDEM (30 m), MERIT
53 DEM (90 m), and ALOS DEM (12.5 – 30 m). While coarse resolution DEM (>30m) are suitable for simulating large-scale
54 flood events in large basins, they are less effective in capturing the detailed topographic features of mountainous terrains or
55 complex urban settings (Saksena and Merwade, 2015; Ogania et al., 2019; Utlu and Özdemir, 2021). Developed countries have
56 leveraged satellite- and airborne-based technologies such as LiDAR or synthetic aperture radar (SAR) to generate Digital
57 Terrain Models (DTMs) and Digital Surface Models (DSMs) with enhanced topographic detail, achieving resolution accuracy
58 down to the centimeter scale (Md Ali et al., 2015).

In recent years, rapid advancements in drone technology have significantly improved the capabilities of civilian small-scale drones. Equipped with features such as flight path planning, automatic flight control, and mountable sensors, these drones have overcome many limitations of traditional surveying equipment, including poor portability, high operational complexity, and cost. Civilian drones are now widely utilized across fields such as hydrology, agriculture, and forestry (Castaldi et al., 2017; Loladze et al., 2019; Acharya et al., 2021). Drones enable the acquisition of the high-resolution digital terrain without being constrained by time or geographic location, and they can be deployed on demand, providing reliable terrain data for precise 2D hydrodynamic model simulations of flood inundation (Meesuk et al., 2015; Cook, 2017). Currently, there are two mainstream methods for obtaining high-precision DEMs using drones. One approach is to use photogrammetry techniques to derive the DEM from drone-borne imagery. This method has relatively lower equipment and processing costs, making it more widely applicable; however, its accuracy is limited in areas with dense vegetation and often requires the establishment of ground control points. The other approach involves using drones equipped with LiDAR to obtain DEMs. This method has the advantage of penetrating vegetation and can acquire high-precision terrain data under all weather conditions, but it comes with higher equipment and processing costs(Muthusamy et al., 2021; Acharya et al., 2021; Naranjo et al., 2021). In theory, as long as the model can process high-resolution DEMs, higher resolution data will yield more accurate simulation results (Muthusamy et al., 2021). However, when obtaining and processing high-resolution DEMs over large areas, practical challenges arise due to drone endurance limitations and the increased computational burden. These challenges grow as the required resolution for flood simulations increases, posing difficulties for researchers and professionals who are not experts in surveying field (Abily et al., 2016). Therefore, rather than pursuing the highest possible resolution, achieving an optimal balance between simulation accuracy and efficiency is critical to meeting the model's requirements (Xing et al., 2018).

Since the introduction of remote sensing imagery into hydraulic modeling, the impact of digital terrain data resolution on flood simulations has become a key area of research. Saksena and Merwade (2015) employed resampling technique and hydraulic model to analyse the relationship between a series of DEM resolutions from 3m to 100m and the extent of flood inundation in different rivers. Their findings demonstrated a positive linear correlation between DEM resolution, water surface elevation, and inundation extent—where coarser resolutions result in larger inundation areas, often leading to over-prediction. However, the applicability of this conclusion is limited to specific rivers and watershed characteristics. Some researchers found that when it comes to surface flooding (such as roads and towns along rivers), the relationship between DEM resolution and flood characteristic simulation results (such as range and depth) is not strictly linear. Moreover, studies have shown that even when DEM resolution is held constant, simulation results can vary significantly depending on the source of the terrain data. Saksena

and Merwade (2015) found that flood simulation results using 30m DEM resampled from LiDAR DEM weremore accurate than those derived from publicly available 30m DEMs based on satellite imagery. These studies all underscore the need to account for the characteristics of the target area and data source when assessing the effect of terrain data resolution on flood simulations to enhance the applicability of conclusions (Shen and Tan, 2020).

Most previous studies have predominantly focused on comparing errors in flood simulation characteristics (inundation area, depth), with limited exploration of the underlying causes of these errors when using different resolution data(Muthusamy et al., 2021). The researches have mainly revolved around spatial and statistical comparisons between simulation results based on different resolution terrain data and benchmark conditions, which are typically derived from high-resolution satellite historical flood inundation maps, simulation results using high-precision terrain resolutions, or field investigation outcomes(Ozdemir et al., 2013; Yalcin, 2020). For fluvial flood modeling in mountainous cities, the variance of river floodplains, riverfront roadways, city streets, and structures with the undulation of the mountains should be the primary elements affecting water flow. Given the cost and challenges of acquiring high-resolution terrain data, more extensive research has typically concentrated on developed plains or coastal cities (Henonin et al., 2015; Xing et al., 2018; Leitao and De Sousa, 2018). These studies generally conclude that drainage network density, building size, and the spatial gaps between structures in DEMs of varying resolution impact flood simulations. However, such conclusions are difficult to generalize to mountainous riverside cities, where terrain undulation and rapid fluctuations in river levels exert a more significant influence on flood process.

The objectives of this study are to: (a) discuss the application of high-resolution DTMs obtained by drones for fluvial flood modeling in the mountainous city; (b) use resampling techniques to examine the effect of DTMs obtained by drones at different resolutions on fluvial flood inundation simulation in the mountainous city; (c) analyse the representation of terrain features by DTMs at different resolutions based on topographic attributes, and investigate the fundamental causes of the effect. Ultimately, this study aims to provide support for the appropriate DTM resolution needed for fluvial flood modeling in mountainous cities.

2 Materials and methods

2.1 study area

The study area, Xuanhan, is a mountainous city in southwestern China, located at the southern foothills of the Daba Mountain range. The built-up area of its main city is 23 km^2, with a population of approximately 153,000. The city is located at the head

of Zhou River, a primary tributary of the Qujiang River Basin, where the Qian River, Zhong River, and Hou River converge. At the confluence, a large reservoir was completed and operational by 1992, with a regulation capacity of 102 million m^3 (Fig. 1). The city has an average annual rainfall of 1248 mm, with over 80% of the total precipitation occurring during the rainy season, primarily between July and September, influenced by the storm-prone Daba Mountain region. Between 1949 and 2021, Xuanhan city experienced 14 major floods (peak flow of 6000-10000 m^3/s), with particularly severe floods occurring in 1982, 2004, 2005, and 2010 (peak flow exceeding 10000 m^3/s). flooding caused by rainfall in the upper reaches of the Qian, Zhong, and Hou Rivers, along with discharges from Jiangkou Reservoir, has resulted in direct economic losses exceeding 2 billion RMB (approximately 279 million USD).

As can be seen from the satellite map in Fig. 1, it can be seen that the study area is surrounded by water on three sides. The urban development axis aligns with the direction of the river, with buildings constructed close to the wide river channel, distributed along the slopes with significant elevation differences. Due to land use constraints, there is no clear buffer zone between the river and the urban area, making it a typical mountainous riverside city. In accordance with the 2022 Flood Control Plan of Xuanhan (Xuanhan County People's Government, 2022), this study delineates a drone survey and flood inundation simulation area that extends along the river to the left and right banks. This area covers six warning points, which correspond to the discharge flows from Jiangkou Reservoir and the city's inundation points, as detailed in Fig. 1 and Table 1.

Taking inundation point A as an example, its specific meaning is: when the flood flow reaches 12,700 m^3/s, the flood will inundate the location of the original Tax Bureau's main gate. The actual representation of an inundation point is the flood boundary line. The determination of each inundation point is based on historical observations and verifications from the flood management department during multiple flood events. During the flood season, personnel from the management department are stationed at these locations to monitor the situation and supervise the evacuation process. The actual flood boundary lines of each inundation point are provided by the local flood disaster management department. We have verified these inundation boundaries through investigations of historical flood traces and interviews with local residents, and they are used for subsequent inundation simulation validation. The selected flood event is a typical flood process measured by the local hydrological bureau based on the 2005 extreme flood event. This flood process includes flow values corresponding to the six inundation points.

The river in the study area is situated in the lowest part of the terrain, with impermeable roads and various buildings constructed along the slopes on both sides. During a flood, the inundation area rapidly spreads from the river channel towards the riverbanks,

with the majority of human and economic losses occurring near the riverbanks. The flood then quickly recedes along the impermeable road surfaces on the slopes of the riverbanks, returning rapidly to the river channel. The impact of the urban drainage network during this process is relatively minor. Additionally, the large Jiangkou Reservoir, located near the study area, significantly blocks sediment from the upstream flow during floods (Winton et al., 2019). The main objective of this study is to assess the impact of terrain data resolution; therefore, the influence of the urban drainage network and sediment transport is not considered in the flood simulation.

2.2 drone images acquisition and processing for generating DSM and DTM

The general workflow for drone image acquisition and processing is outlined in Fig. 2.The drone flight campaign took place on January 10, 2023, during the winter dry season, when the study area experienced low river depths and exposed riverbeds. The DJI Matrice 300 RTK equipped with a Ruibo five-lens oblique photography sensor was used for the drone survey. The DJI Pilot 2 software was employed for flight control, enabling the automatic configuration of flight paths and shooting parameters. In order to minimize the effects of building obstructions within the survey area, the flight altitude was set at 200 meters, with image overlaps configured at 80% for the longitudinal direction and 70% for the side direction (Cunliffe et al., 2016). A total of 1,467 vertical images were captured, achieving a ground sample distance of 3 cm..

The ground control points (GCPs) were established using a Hi-Target Global Navigation Satellite Systems (GNSS) receiver in Real-Time Kinematic (RTK) positioning mode. DJI Terra software was utilized to process the drone images, incorporating five control points to optimize sensor position and orientation data, as well as to verify positional accuracy. The final output products included orthoimages and an initial DSM. To ensure the preservation of spatial details, the "highest quality" processing option was selected when using DJI Terra to process the imagery (i.e., selecting the highest point cloud density and feature points). This option imposes certain requirements on the computer hardware. The hardware specifications used in this study are shown in Table 2, and the initial DSM accuracy achieved was 6 cm.

DSM (Digital Surface Model) represents the elevation data of all visible surface features, including vegetation, buildings, and overhead power lines. To achieve accurate hydraulic modeling, it is typically necessary to filter out these surface features from the DSM to generate a DTM (Digital Terrain Model), which focuses only on the natural terrain without surface features. In this study, PCI Geomatica software was used to filter vegetation, water surfaces, and noise from roads in the initial DSM. All buildings along the riverbank were preserved to meet the requirements for flood inundation simulation. PCI Geomatica allows manual local editing of the DSM, which is a better option for our study area, as the vegetation is relatively small and dispersed.

Compared to global filtering of the entire study area, local processing is more suitable and results in higher DTM accuracy. The specific processing workflow is as follows:

Step 1: Import the initial DSM, open the DEM Editor, and create a new polygon layer. Select the local area to be filtered (Fig. 3a).

Step 2: Select the Average Filter to smooth the local area and initially reduce noise effects, making the filtered area transitions more natural.

Step 3: Use the Pit and Bump Filter, selecting remove bump and remove pit to filter local undulations and bumps in the area, mainly targeting mid- to low-elevation vegetation and noise on exposed riverbeds. This step requires alternating between remove bump and remove pit multiple times, adjusting the filter parameters (size and gradient, which control the size and shape of the objects to be filtered) appropriately. The parameters are gradually adjusted from large to small until the filtered area becomes smooth and shows no further changes (Fig. 3b).

Step 4: Apply the Terrain Filter to remove residual visible features that are difficult to filter, such as taller vegetation. Terrain Filters focus on overall topographic features, and since buildings are retained for flood inundation simulation, care should be taken to avoid selecting buildings when filtering the area (Fig. 3c).

Step 5: Use the Median Filter to smooth rough edges from the previous steps. This step will not remove any remaining bumps or pits.

Step 6: After filtering one area, select the next area and repeat the steps above until all noise, except buildings along the riverbank, has been filtered out. The final output is the DTM that can be input into the hydraulic model.

The DTM was subsequently resampled to coarser resolutions of 1 m, 5 m, 10 m, 15 m, and 30 m for further analysis.

Traditionally, in shallow water areas, bathymetric measurements are taken by operators using RTK-GNSS receiver while wading through the water. In deeper waters, bathymetric measurements are typically conducted using sonar instruments mounted on manned or unmanned vessels. Research on drone-borne sensors for bathymetric measurements has also made significant progress, such as with drone-borne ground penetrating radar or blue-green LiDAR. Although these methods require certain conditions for water depth and clarity, they have demonstrated superior performance to traditional sonar methods in specific scenarios, showing substantial potential in practical applications (Bandini et al., 2023; Mandlburger et al., 2020; Bandini et al., 2018; Pan et al., 2015). In this study, measurements were conducted during the winter low-flow period, when river depths are shallow, and large areas of riverbed are exposed. As such, unmanned boats equipped with single-beam sonar were used to measure underwater cross-sections in the non-dried sections of the river.

Based on the research of Zhao et al. (2017), during the dry season, drone imagery could be used to capture the downward trend

of the exposed river floodplains on both sides of the river cross-section. By integrating the measured water depths, the underwater cross-sections of the river were generalized into rectangular, trapezoidal, or arc-shaped profiles(Fig.4). The complete underwater terrain data was then obtained through cross-section interpolation. This interpolation correction was carried out using the terrain processing tool RAS Mapper in HEC-RAS. The tool uses linear interpolation to modify the underwater terrain between the measured cross-sections and generate a new terrain model. This terrain model can then be combined with the general surface terrain model (which does not accurately depict the terrain below the water surface) to create an improved terrain model for hydraulic modeling and mapping (U.S. Army Corps of Engineering, 2016).

2.3 Flood inundation modeling

The hydraulic model used in this study is the Hydrologic Engineering Center's River Analysis System (HEC-RAS) model, version 6.3.1. HEC-RAS is developed by the Hydrologic Engineering Center of the U.S. Army Corps of Engineers (U.S. Army Corps of Engineering, 2016). This software allows you to perform one-dimensional steady flow, one- and two-dimensional unsteady flow hydraulics modeling, sediment transport/mobile bed computations, water temperature modeling, and generalised water quality modeling (U.S. Army Corps of Engineering, 2016). It is one of the most widely used hydraulic models globally that is publicly available. This model includes two computational solvers, the two-dimensional Saint-Venant equations (Equation 1) and the two-dimensional diffusion wave equation (Equation 2). The vector forms of the momentum equations are as follows:

$$\frac{\partial \boldsymbol{V}}{\partial t} + (\boldsymbol{V}\cdot\nabla)\boldsymbol{V} + f_c\boldsymbol{k}\times\boldsymbol{V} = -g\nabla z_s + \frac{1}{h}\nabla\cdot(\boldsymbol{\nu}_t h\nabla\boldsymbol{V}) - \frac{\boldsymbol{\tau}_b}{\rho R} + \frac{\boldsymbol{\tau}_s}{\rho h} - \frac{1}{\rho}\nabla p_a \quad (1)$$

$$\frac{gn^2}{R^{4/3}}|\mathbf{V}|\mathbf{V} = -g\nabla Z_s - \frac{1}{\rho}\nabla p_a + \frac{\tau_s}{\rho h} \quad (2)$$

where here the velocity vector (m/s) is $\boldsymbol{V} = (u, v)^T$, $\boldsymbol{\nu}_t$ is the horizontal eddy viscosity coefficient tensor (m^2/s), ∇ is the gradient operator (1/m), $\boldsymbol{k}$ is the unit vector in the vertical direction (dimensionless), $\boldsymbol{\tau}_b$ and $\boldsymbol{\tau}_s$ is the bottom shear and wind surface stress vector ($kg\cdot m/s^2$), h is water depth (m), f_c is coriolis parameter (1/s), p_a is atmospheric pressure ($kg\cdot m/s^2$), R is hydraulic radius (m), Z_s is water surface elevation (m), g is gravitational acceleration (m/s^2), n is manning's roughness coefficient ($s/m^{1/3}$), ρ is water density (kg/m^3).

The 2D unsteady flow equation solvers both use the implicit finite volume solution algorithm. The implicit solution algorithm allows for a larger computational time step than explicit methods. Compared with traditional finite difference and finite element techniques, the finite volume method significantly improves the stability and robustness of the solution process (Mourato et al., 2021). For specific model introductions and usage, please refer to the HEC-

RAS Applications Guide and HEC-RAS User's Manual (U.S. Army Corps of Engineering, 2016).

The flood inundation modeling in this study used a full two-dimensional unsteady flow model. Fig. 5 shows the topographic data of the area, the two-dimensional computational grid, and the upstream and downstream boundary conditions (represented by the blue line in Fig. 5). For the model's upstream boundary, the input data consisted of a typical flood hydrograph with a time step of 1 hour. The downstream boundary conditions were defined using the normal water depth, calculated based on the river slope . The downstream river slope, derived from the drone-obtained DTM, was determined to be 0.00084 m/m.The detailed model setup is presented in Table 3.

The computational time for 2D flood inundation simulations using HEC-RAS is primarily related to two factors: the 2D flow calculation and floodplain mapping. The computational time for 2D flow is associated with the computational mesh size setting and is less influenced by the resolution of the terrain data. Yalcin (2020) found that significant fluctuations in the results of the 2D flow calculations only appear when the computational mesh size exceeds 15 m x 15 m. Given that the main objective of this study is to assess the impact of DTM resolution, a computational mesh with 5 m x 5 m cells was used for all simulations. In contrast, floodplain mapping is based on terrain data, and its computational efficiency and drawing accuracy are directly related to the DTM resolution. Selecting an appropriate DTM resolution is crucial for the timeliness and reliability of flood risk analysis. Table 4 shows the computational results for floodplain mapping using different DTM resolutions, and the hardware specifications used for the simulations are shown in Table 2.

2.4 Topographic attributes analysis

Obtaining topographic attributes from digital terrain data is a common approach for capturing digital terrain features, evaluating terrain data quality, and analyzing the uncertainty in terrain representation at different resolutions. More than ten commonly used topographic attributes are employed in various fields such as hydrological analysis, land use, and soil-vegetation studies. Each indicator uses different methods to describe the terrain structure and shape, and the undulation of the terrain directly affects the flow of water on the surface. In this study, six topographic attributes closely associated with hydraulic simulation and hydrological analysis were selected to evaluate the effects of DTMs at different resolutions on flood inundation simulation. The topographic attributes are: Elevation, Topographic Position Index (TPI), Terrain Ruggedness Index (TRI), Wind Exposition Index (WEI), Morphometric Protection Index (MPI), Vector Ruggedness Measure (VRM). The detailed

definitions of these attributes are shown in Table 5.

Salekin et al. (2023) demonstrated that when extracting topographic attributes, using the average value across the plot is more representative than directly measuring the center point, as the latter lacks spatial representativeness. Therefore, this study established 894 square plots of 30 m x 30 m in the analysis area based on the coarsest resolution (30m) as the plot side length. This approach ensures that at the coarsest resolution, the calculation of the plot contains complete grid pixels, and at a finer resolution, each plot can contain multiple complete grid pixels. All geospatial processing and data extraction were performed using ArcGIS and the System for Automated Geoscientific Analysis (SAGA v8.5.1) (Conrad et al., 2015). The Mean Absolute Error (MAE) was used to analyse the differences in DTM topographic attributes at different resolutions:

$$\mathrm{MAE} = \frac{1}{m}\sum_{i=1}^{m}|x_i - y| \quad (3)$$

Where m is the total number of plots calculated, x_i is the average value of the topographic indicators of each plot in the resampled DTM and y is the topographic attribute value as a benchmark and control value, i.e., the value of topographic attributes of the 6cm DTM obtained by the drone.

3 Results and discussion

3.1 Performance of drone DTM in mountainous urban fluvial flood modeling

For most flood events, obtaining real, accurate, and complete flood inundation maps (including inundation extent and flood depth) for model validation is highly challenging. In this study, six inundation warning points provided by the local flood disaster management department were used for validation. Based on years of manual observations made by management department personnel at these points during the flood season, combined with investigations of historical flood traces and interviews with local residents, the historical flood inundation boundary lines for each point were delineated (Fig. 6). The six images on the inner side of Fig. 6 are field survey images of the six inundation points. The red lines in the images represent the delineated historical inundation boundaries, which were used to validate the simulated flood inundation extent (i.e., to assess whether the simulated flood boundary coincides with the red historical inundation boundary). During the simulation process, in order to ensure accurate representation at the six inundation points, a 20% upward adjustment was made to the Manning's coefficient for both the river channel and the riverbanks.

The flood simulation results based on the 6 cm DTM are shown in Fig. 6 and Fig. 7. The six localized magnified orthophotos in the outer part of Fig. 6 represent the corresponding flood mapping results from HEC-RAS at the six inundation points. The

red lines in the localized magnified orthophotos are consistent with the red lines in the field photos. From the HEC-RAS 2D simulation results, the simulated flood inundation at the six points aligns well with the historical flood inundation boundary lines. Since the elevation positions of the six inundation points increase with the corresponding flood flow values, and their distribution covers the upper, middle, and lower sections of the study area, it indicates a good agreement between the flood simulation based on high-precision terrain data (6 cm DTM) and the actual flood inundation. Therefore, the calibrated model results obtained with the 6 cm DEM are considered benchmark conditions for subsequent spatial and statistical comparative analysis based on different resolutions. The final benchmark flood inundation area was 76.47 ha, with a maximum flood depth of 24.39 m, a minimum depth of 0.01 m, and an average depth of 18.09 m (Fig. 7)

.3.2 Effects of different resolutions on flood modeling

3.2.1 Overall comparison of flood area and depth

The resampled DTMs (1 m, 5 m, 10 m, 15 m, and 30 m) were sequentially input into the HEC-RAS for flood inundation modeling. The simulation results were compared with the benchmark (6 cm DTM) both spatially and statistically. The inundation area of the benchmark was overlaid with the inundation boundary polygons from simulations based on other resolutions for comparative analysis. For inundation depth, the ArcGIS raster calculator was used to output the difference between the inundation depth raster maps, enabling pixel-by-pixel comparisons. The pixel-based differences (i.e., errors) were then used to evaluate the simulation performance based on DTMs of different resolutions, using statistical metrics such as the Mean Absolute Error (MAE) and Root Mean Square Error (RMSE). Fig. 8 shows the spatial and statistical comparison of flood inundation from simulations at different DTM resolutions with the benchmark (6 cm DTM) under the maximum flood peak flow (12700 m^3 /s).

As shown in Fig. 8, it can be seen that as the DTM resolution decreases, the inundation area shows a decreasing trend compared to the benchmark, especially when using 10 m DTM or coarser resolution DTMs, where noticeable differences in inundation extent appear on the riverbanks outside the main river channel. Many areas of significant flood extent mismatch are evident. For flood depth difference, the discrepancies become more pronounced when using 10 m and 15 m DTMs. This observation is supported by both statistical values and the clear spatial distribution changes. Additionally, the flood depth difference shows varying degrees of change both within the main river channel and along the floodplain and riverbanks.

Fig. 9 shows the variation trend in inundation area and mean flood depth at maximum flood peak flow (12700m^3/s) based on DTMs at different resolutions. As shown in Fig. 9a, within the main river channel, there is no distinct trend in the inundation

area as the DTM resolution decreases, with only slight fluctuations observed. While the mean flood depth shows an obvious fluctuation when the resolution is greater than 5 m. The absence of significant trends in the modeling results within the main channel can be attributed to the coarsest resolution (30 m) being much smaller than the average river width (around 182 m) in the study area . Meanwhile, except for the exposed riverbed topographic data obtained by drone during the dry season, the rest of the underwater topography of the river channel was obtained by generalised cross-section interpolation based on the trend of the floodplain (obtained by the drone) combined with the maximum underwater depth (obtained by the unmanned boat), which has a limited capture of the undulating features of the underwater topography, resulting in insensitivity to DTM resolution changes in the main river channel inundation simulation. Although no clear change pattern emerges, the fluctuations in the results indicate that the impact of DTM resolution on flood inundation simulation is not a simple linear relationship.

As shown in Fig. 9b, the floodplain and riverbank areas outside the main channel exhibit a notable decreasing trend in inundation area as the DTM resolution decreases. Using the flood modeling result from the 6 cm DTM as a benchmark, the inundation area reduces by 0.65%, 1.62%, 3.38%, 4.25%, and 7.67% for DTM resolutions of 1 m, 5 m, 10 m, 15 m, and 30 m, respectively. While the mean flood depth remains relatively unchanged at 1 m and 5 m DTMs, a clear increasing trend is observed beyond 5 m resolution, with the mean flood depth rising by 2.21%, 4.31%, and 10.41% at DTMs of 10 m, 15 m, and 30 m, respectively. Overall, both the inundation area and mean flood depth exhibit distinct step changes. Specifically, compared to the benchmark, the magnitude of change is minimal and similar at 1 m and 5 m DTMs, more substantial yet similar at 10 m and 15 m DTMs, and greatest at 30 m DTM. The dashed lines in Fig. 9b were used to better depict the variations (step changes) between the simulation results at different resolutions.

In the floodplains and riverbank areas of the mountainous city, as the DTM resolution decreases, the simulated inundation area decreases, while the mean flood depth increases. This indicates that changes in resolution significantly affect the characterization of DTM topography. Notably, both the flood area and depth showed some stage changes in the whole mountainous urban fluvial flood modeling as shown in Fig. 9 and this was also supported by visualising inundation area at different DTM resolutions (Fig. 6). The possible reason for this phenomenon is that as the resolution becomes coarser, the topographic undulation of the inundation area changes from the original smooth trend to a step-like trend, altering the flood inundation process in the model. This step-like trend of topographic undulation also makes the relationship between resolution change and flood inundation characteristics present a non-linear relationship (step change). As the resolution decreases beyond a certain threshold, these step-like changes in topography can become increasingly pronounced.

3.2.2 Specific effects of different resolution the inundation points

To further analyse the effect of DTM resolution on mountainous urban fluvial flood modeling, we evaluated the simulation results at six inundation points across different DTM resolutions. As an example, Fig. 10 illustrates the inundation modeling results at point C(11200m^3/s) produced by using different DTM resolutions. The inundation scenario simulated with the 6 cm DTM was treated as the benchmark for comparison, with the red line in Fig. 10 representing the benchmark inundation boundary lines. By comparing the modeling results of different resolutions at point C, the simulations based on the 1 m and 5 m DTMs demonstrated the best alignment with the benchmark boundary, with nearly identical inundation extents. In contrast, the simulations using the 15 m and 30 m DTMs showed poorer performance, as the modeled inundation boundaries deviated significantly from the benchmark. The inundation boundary simulated using the 10 m DTM slightly exceeds the boundary line of the benchmark. While the boundaries nearly coincided, the modeled flood depth at 10m resolution was greater than the benchmark (the colour is deeper than the benchmark).

Using the inundation border lines of the six inundation points simulated with the 6 cm DTM (represented by the red lines in Fig. 8) as the benchmark, the red benchmark lines were converted into points based on the flood inundation depth raster maps using ArcGIS. Each point corresponds to the flood depth value of the associated pixel. These points were then used to extract the corresponding flood depth from the flood inundation depth raster maps at different resolutions (if a point falls on a grid cell with no inundation data, the flood depth is set to 0). The pixel-based flood depths were subtracted from the benchmark flood depths to calculate the mean error. Table 6 presents the comparison of simulation results at six inundation points using DTMs of different resolutions with the benchmark, with the values in the table representing the average error in flood depth between the simulated inundation boundaries and the benchmark.

A horizontal comparison of the results in Table 6 reveals that as the simulated discharge increases, he influence of DTM resolution on the accuracy of inundation simulation becomes more pronounced. For the minimum discharge of 6000m^3/s (point F), the inundation boundaries simulated using DTMs ranging from 1 m to 15 m resolution align closely with the benchmark boundary (green color in the table). However, at the maximum discharge of 12700m^3/s (point A), only the simulation result using the 1 m DTM is in agreement with the benchmark. For those points where the simulated inundation boundary does not coincide with the benchmark, the average distance between the simulated boundary and the reference boundary generally increases as the resolution becomes coarser.

A vertical comparison of simulation results at different resolutions in Table 6 indicates that the inundation boundary simulated using a 1 m DTM is in perfect coincidence with the benchmark, exhibiting minimal error in flood depth wit an average error of 0.04m. The inundation boundaries produced using 5 m and 10 m DTMs are basically consistent with the benchmark at all inundation points except at some extreme discharges, but the flood depth simulated using a 10 m DTM is much greater than the depth at finer resolutions. When 5 m and 10 m DTMs are utilized to determine the qualified inundation border, the average flood depth errors are 0.048 m and 0.392 m, respectively. It is clear that DTMs of 15 m and 30 m cannot meet the requirements for mountainous urban fluvial flood modeling.

Considering the results of Fig. 10 and Table 6, it can be seen that the simulation effect of flood characteristics shows a certain step change with the change of DTM resolution in the mountainous urban fluvial flood modeling. Specifically, when the resolution is greater than 10 m, the simulation results of its flood characteristics cannot meet the requirements for accurately modeling flood inundation in riverside mountainous cities. When the resolution is maintained at or below 5 m, the simulation outcomes largely fulfill the necessary criteria, with the results from a 1 m DTM aligning closely with those derived from centimeter-level DTM simulations. Although the results obtained using a 10 m DTM are generally acceptable concerning inundation boundaries, they tend to overestimate flood depth compared to the simulations conducted with 1 m and 5 m DTMs

3.3 Analysing the causes of effects based on topographic attributes

Floods in mountainous riverside cities are mainly caused by rapid confluence of flash floods driven by heavy rain. To further analyse the fundamental reasons for the impact of different resolution DTMs on flood inundation simulation in mountainous riverside cities, six topographic attribute indicators, namely, elevation, TPI, TRI, WEI, MPI, and VRM were selected to statistically analyse the topographic attributes of DTMs at different resolutions. Table 7 presents the statistical results of the topographic features derived from the 6 cm DTM, reflecting the topographic undulation of the study area from multiple perspectives. For example, TPI quantifies the height difference between a grid cell and the average height of its surrounding grid cells, with values ranging from -2.87 to 28.51 and an average close to 0. This indicates significant topographic variation in the area, characterized by distinct distributions of elevated and depressed landforms. The filtered DTM retains buildings for flood modeling, so variables such as WEI, MPI, or VRM that describe steep ridge sites as well as accumulation areas can also be used to characterize the DTM's representation of mountainous buildings and bare ground.

Using the topographic attributes derived from the 6 cm DTM as a benchmark, this study analyzed the characterization of

topographic attributes in the study area as represented by DTMs with resolutions ranging from 1 m to 30 m. Fig. 11 illustrates the distribution of absolute errors for the six topographic attribute metrics calculated across 894 square plots, while Table 8 presents the final Mean Absolute Error (MAE) values. The results show that as the resolution of the DTM becomes coarser, the overall error between the six topographic attribute indicators and the benchmark increases. As shown in Fig. 9(a), (d), (e), and (f), the four indicators (elevation, WEI, MPI, and VRM) exhibit a significant step change around a resolution of 10 m, with errors for the 5 m and 10 m DTMs being relatively similar. However, for the remaining two indicators(TPI and TRI), the error associated with the 10 m DTM is substantially greater than that associated with the 5 m DTM. This discrepancy suggests the existence of a threshold regarding the effects of DTM resolution changes on topographic attributes. DTMs with resolutions below 10 m are more effective in capturing the undulating features of the topography in the study area, which is critical for accurately modeling the inundation area. However, for features characterized by specific elevation differences, such as TPI and TRI, it is advisable to maintain a resolution of 5 m or finer, as this will directly influence the accuracy of flood depth modeling.

In conjunction with the earlier analysis of flood inundation simulations, it was found that as the resolution changes, there is consistency between the simulation results of flood inundation characteristics and the changes in topographic attributes. This consistency indicates that the effect of DTM resolution on inundation modeling is mainly related to the complexity and undulation of the terrain, and the simulation accuracy is directly related to whether the DTM can accurately capture topographic features. The analysis of topographic attributes provides theoretical support for obtaining the optimal resolution to match simulation requirements. For mountainous urban fluvial flood modeling, utilizing the DTM obtained by drones as the terrain input, the resolution within 10 m can basically meet the simulation needs of the inundation area, since the DTM within this resolution can accurately characterise the features of the undulating and complex terrain (including buildings). However, considering the simulation needs of the flood depth and balancing the computational cost and the simulation requirements, the resolution of 1 m to 5 m can present better results, since the DTM with this resolution can accurately capture the characteristics of the specific difference in the elevation.

4 Conclusion

This study conducted a 2D flood inundation simulation for a mountainous riverside city in southwest China, utilizing high-precision DTM obtained by drone. Considering the local government's flood prevention plan, field investigation of historical inundation traces, and inundation boundaries, the flood inundation simulation area and six inundation points for model

validation were determined. The results showed that the flood inundation simulation and the historical flood inundation boundary lines at the six inundation points were well matched, and there was a good consistency between the model simulation results and the actual flood inundation.

The 6 cm DTM obtained by drone was resampled into 1 m, 5 m, 10 m, 15 m and 30 m DTM, respectively, as the terrain input for the 2D flood inundation simulation, and the effect of different resolutions on mountainous urban fluvial flood modeling was discussed. The results showed that, in the floodplain and riverbank outside the main channel, the inundation area showed a significant decreasing trend with the decrease of resolution. The mean flood depth did not change significantly at 1 m and 5 m DTM, but showed a significant increasing trend after the resolution was greater than 5 m. Both inside and outside the river channel showed a certain step change.

Similarly, based on the 6 cm DTM as the benchmark, the characterisation of topographic attributes by different resolution DTMs was further analysed. We found that there was a certain threshold for the effect of DTM resolution on topographic attributes. Compared with the DTM with a resolution of more than 10 m, the DTM with a resolution of less than 10 m could better capture the undulating and complex terrain features of the study area, especially within 5 m.

According to the analysis of terrain attributes, using the DTM obtained by drone to conduct a mountainous urban fluvial flood modeling, the resolution of the terrain data used should be kept within 1 m to 5 m. However, if larger watersheds and larger mountainous cities were involved, in the case of non-extreme discharges, considering the cost of acquisition and processing, using a resolution of 5 m to 10 m could also meet certain requirements in terms of inundation area drawing, but there could be a possibility of overestimation of flood depth.

Data availability. The hydrological data used in this study were provided by Sichuan Dazhou Hydrological and Water Resources Survey Centre.

Author contribution. XZ, TA, and XH suggested the idea and formulated the overarching research goals and aims. XY and XH operated the drone to get the image data. XZ, LM, and HY processed, corrected and managed the data. XZ prepared the manuscript with contributions from all co-authors.

Competing interests. The contact author has declared that neither they nor their co-authors have any competing interests.

460

461 *Disclaimer.* The opinions expressed here are those of the authors and not those of other individuals or organizations.

462

463 *Financial support.* This research has been supported by Sichuan University-Dazhou Municipal People's Government Strategic
464 cooperation special fund project (grant nos. 2021CDDZ-12).

465 **Reference**

466 Abily, M., Bertrand, N., Delestre, O., Gourbesville, P., and Duluc, C.-M.: Spatial Global Sensitivity Analysis of High
467 Resolution classified topographic data use in 2D urban flood modeling, Environ. Modell. Softw., 77, 183-195,
468 https://doi.org/10.1016/j.envsoft.2015.12.002, 2016.
469 Acharya, B. S., Bhandari, M., Bandini, F., Pizarro, A., Perks, M., Joshi, D. R., Wang, S., Dogwiler, T., Ray, R. L., Kharel, G.,
470 and Sharma, S.: Unmanned Aerial Vehicles in Hydrology and Water Management: Applications, Challenges, and Perspectives,
471 Water Resour. Res., 57, https://doi.org/10.1029/2021WR029925, 2021.
472 Alderman, K., Turner, L. R., and Tong, S.: Floods and human health: A systematic review, Environ. Int., 47, 37-47,
473 https://doi.org/10.1016/j.envint.2012.06.003, 2012.
474 Azizian, A. and Brocca, L.: Determining the best remotely sensed DEM for flood inundation mapping in data sparse regions,
475 Int. J. Remote Sens., 41, 1884-1906, https://doi.org/10.1080/01431161.2019.1677968, 2020.
476 Bandini, F., Kooij, L., Mortensen, B. K., Caspersen, M. B., Thomsen, L. G., Olesen, D., and Bauer-Gottwein, P.: Mapping
477 inland water bathymetry with Ground Penetrating Radar (GPR) on board Unmanned Aerial Systems (UASs), J. Hydrol., 616,
478 10.1016/j.jhydrol.2022.128789, 2023.
479 Bandini, F., Olesen, D., Jakobsen, J., Kittel, C. M. M., Wang, S., Garcia, M., and Bauer-Gottwein, P.: Technical note:
480 Bathymetry observations of inland water bodies using a tethered single-beam sonar controlled by an unmanned aerial vehicle,
481 Hydrol. Earth Syst. Sci., 22, 4165-4181, 10.5194/hess-22-4165-2018, 2018.
482 Bates, P. D.: Integrating remote sensing data with flood inundation models: how far have we got?, Hydrol. Processes, 26, 2515-
483 2521, https://doi.org/10.1002/hyp.9374, 2012.
484 Castaldi, F., Pelosi, F., Pascucci, S., and Casa, R.: Assessing the potential of images from unmanned aerial vehicles (UAV) to
485 support herbicide patch spraying in maize, Precis. Agric., 18, 76-94, https://doi.org/10.1007/s11119-016-9468-3, 2017.
486 Conrad, O., Bechtel, B., Bock, M., Dietrich, H., Fischer, E., Gerlitz, L., Wehberg, J., Wichmann, V., and Boehner, J.: System
487 for Automated Geoscientific Analyses (SAGA) v. 2.1.4, Title Geosci. Model Dev., 8, 1991-2007,

488 https://doi.org/10.5194/gmd-8-1991-2015, 2015.
489 Cook, A. and Merwade, V.: Effect of topographic data, geometric configuration and modeling approach on flood inundation
490 mapping, J. Hydrol., 377, 131-142, https://doi.org/10.1016/j.jhydrol.2009.08.015, 2009.
491 Cook, K. L.: An evaluation of the effectiveness of low-cost UAVs and structure from motion for geomorphic change detection,
492 Geomorphology, 278, 195-208, https://doi.org/10.1016/j.geomorph.2016.11.009, 2017.
493 Corringham, T. W. and Cayan, D. R.: The Effect of El Nino on Flood Damages in the Western United States, Weather Clim.
494 Soc., 11, 489-504, https://doi.org/10.1175/WCAS-D-18-0071.1, 2019.
495 Cunliffe, A. M., Brazier, R. E., and Anderson, K.: Ultra-fine grain landscape-scale quantification of dryland vegetation
496 structure with drone-acquired structure-from-motion photogrammetry, Remote Sens. Environ., 183, 129-143,
497 https://doi.org/10.1016/j.rse.2016.05.019, 2016.
498 da Costa, R. T., Mazzoli, P., and Bagli, S.: Limitations Posed by Free DEMs in Watershed Studies: The Case of River Tanaro
499 in Italy, Front. Earth Sci., 7, https://doi.org/10.3389/feart.2019.00141, 2019.
500 Güneralp, B., Güneralp, İ., and Liu, Y.: Changing global patterns of urban exposure to flood and drought hazards, Glob.
501 Environ. Change-Human Policy Dimens., 31, 217-225, https://doi.org/10.1016/j.gloenvcha.2015.01.002, 2015.
502 Harris, A. and Baird, A. J.: Microtopographic Drivers of Vegetation Patterning in Blanket Peatlands Recovering from Erosion,
503 Ecosystems, 22, 1035-1054, https://doi.org/10.1007/s10021-018-0321-6, 2019.
504 Henonin, J., Ma, H., Yang, Z.-Y., Hartnack, J., Havno, K., Gourbesville, P., and Mark, O.: Citywide multi-grid urban flood
505 modeling: the July 2012 flood in Beijing, Urban Water J., 12, 52-66, https://doi.org/10.1080/1573062X.2013.851710, 2015.
506 Kumar, L., Skidmore, A. K., and Knowles, E.: modeling topographic variation in solar radiation in a GIS environment, Int. J.
507 Geogr. Inf. Sci., 11, 475-497, https://doi.org/10.1080/136588197242266, 1997.
508 Leitao, J. P. and de Sousa, L. M.: Towards the optimal fusion of high-resolution Digital Elevation Models for detailed urban
509 flood assessment, J. Hydrol., 561, 651-661, https://doi.org/10.1016/j.jhydrol.2018.04.043, 2018.
510 Loladze, A., Augusto Rodrigues, F., Jr., Toledo, F., San Vicente, F., Gerard, B., and Boddupalli, M. P.: Application of Remote
511 Sensing for Phenotyping Tar Spot Complex Resistance in Maize, Front. Plant Sci., 10, https://doi.org/10.3389/fpls.2019.00552,
512 2019.
513 Mandlburger, G., Pfennigbauer, M., Schwarz, R., Floery, S., and Nussbaumer, L.: Concept and Performance Evaluation of a
514 Novel UAV-Borne Topo-Bathymetric LiDAR Sensor, Remote Sens., 12, 10.3390/rs12060986, 2020.
515 Md Ali, A., Solomatine, D. P., and Di Baldassarre, G.: Assessing the impact of different sources of topographic data on 1-D
516 hydraulic modeling of floods, Hydrol. Earth Syst. Sci., 19, 631-643, https://doi.org/10.5194/hess-19-631-2015, 2015.
517 Meesuk, V., Vojinovic, Z., Mynett, A. E., and Abdullah, A. F.: Urban flood modeling combining top-view LiDAR data with

ground-view SfM observations, Adv. Water Resour., 75, 105-117, https://doi.org/10.1016/j.advwatres.2014.11.008, 2015.

Mourato, S., Fernandez, P., Marques, F., Rocha, A., and Pereira, L.: An interactive Web-GIS fluvial flood forecast and alert system in operation in Portugal, Int. J. Disaster Risk Reduct., 58, https://doi.org/10.1016/j.ijdrr.2021.102201, 2021.

Muthusamy, M., Casado, M. R., Butler, D., and Leinster, P.: Understanding the effects of Digital Elevation Model resolution in urban fluvial flood modeling, J. Hydrol., 596, https://doi.org/10.1016/j.jhydrol.2021.126088, 2021.

Naranjo, S., Rodrigues Jr, F. A., Cadisch, G., Lopez-Ridaura, S., Fuentes Ponce, M., and Marohn, C.: Effects of spatial resolution of terrain models on modelled discharge and soil loss in Oaxaca, Mexico, Hydrol. Earth Syst. Sci., 25, 5561-5588, 10.5194/hess-25-5561-2021, 2021.

Ogania, J. L., Puno, G. R., Alivio, M. B. T., and Taylaran, J. M. G.: Effect of digital elevation model's resolution in producing flood hazard maps, Glob. J. Environ. Sci. Manag., 5, 95-106, https://doi.org/10.22034/gjesm.2019.01.08, 2019.

Ozdemir, H., Sampson, C. C., de Almeida, G. A. M., and Bates, P. D.: Evaluating scale and roughness effects in urban flood modeling using terrestrial LIDAR data, Hydrol. Earth Syst. Sci., 17, 4015-4030, https://doi.org/10.5194/hess-17-4015-2013, 2013.

People's Government of Xuanhan County: Xuanhan County 2022 Flood Protection Plan, available at http://www.xuanhan.gov.cn/xxgk-show-64349.html (last accesse: January 2024), 2022.

Pan, Z., Glennie, C., Hartzell, P., Fernandez-Diaz, J. C., Legleiter, C., and Overstreet, B.: Performance Assessment of High Resolution Airborne Full Waveform LiDAR for Shallow River Bathymetry, Remote Sens., 7, 5133-5159, 10.3390/rs70505133, 2015.

Saksena, S. and Merwade, V.: Incorporating the effect of DEM resolution and accuracy for improved flood inundation mapping, J. Hydrol., 530, 180-194, https://doi.org/10.1016/j.jhydrol.2015.09.069, 2015.

Salekin, S., Bloomberg, M., Morgenroth, J., Meason, D. F., and Mason, E. G.: Within-site drivers for soil nutrient variability in plantation forests: A case study from dry sub-humid New Zealand, Catena, 200, https://doi.org/10.1016/j.catena.2021.105149, 2021.

Salekin, S., Lad, P., Morgenroth, J., Dickinson, Y., and Meason, D. F.: Uncertainty in primary and secondary topographic attributes caused by digital elevation model spatial resolution, Catena, 231, https://doi.org/10.1016/j.catena.2023.107320, 2023.

Salekin, S., Mason, E. G., Morgenroth, J., Bloomberg, M., and Meason, D. E.: modeling the Effect of Microsite Influences on the Growth and Survival of Juvenile Eucalyptus globoidea (Blakely) and Eucalyptus bosistoana (F. Muell) in New Zealand, Forests, https://doi.org/10, 10.3390/f10100857, 2019.

Samela, C., Manfreda, S., Paola Francesco, D., Giugni, M., Sole, A., and Fiorentino, M.: DEM-Based Approaches for the Delineation of Flood-Prone Areas in an Ungauged Basin in Africa, J. Hydrol. Eng., 21, 06015010,

https://doi.org/10.1061/(ASCE)HE.1943-5584.0001272, 2016.

Shen, J. and Tan, F.: Effects of DEM resolution and resampling technique on building treatment for urban inundation modeling: a case study for the 2016 flooding of the HUST campus in Wuhan, Nat. Hazards, 104, 927-957, https://doi.org/10.1007/s11069-020-04198-z, 2020.

U.S. Army Corps of Engineering: HEC-RAS 5.0 Hydraulic Reference Manual. U.S.Army Corps of Engineers, Institute for Water Resources, Hydrologic Engineering Center, Davis, CA, USA. CPD-68, 2016.

Utlu, M. and Ozdemir, H.: How much spatial resolution do we need to model a local flood event? Benchmark testing based on UAV data from Biga River (Turkey), Arab. J. Geosci., 13, https://doi.org/10.1007/s12517-020-06318-2, 2020.

WHO: World Health Organisation - Flood [WWW Document], available at: https://www.who.int/health-topics/floods#tab=tab_1 (last accesse: December 2023), 2020.

Winton, R. S., Calamita, E., and Wehrli, B.: Reviews and syntheses: Dams, water quality and tropical reservoir stratification, Biogeosciences, 16, 1657-1671, 10.5194/bg-16-1657-2019, 2019.

Xing, Y., Liang, Q., Wang, G., Ming, X., and Xia, X.: City-scale hydrodynamic modeling of urban flash floods: the issues of scale and resolution, Nat. Hazards, 96, 473-496, https://doi.org/10.1007/s11069-018-3553-z, 2018.

Yalcin, E.: Assessing the impact of topography and land cover data resolutions on two-dimensional HEC-RAS hydrodynamic model simulations for urban flood hazard analysis, Nat. Hazards, 101, 995-1017, 10.1007/s11069-020-03906-z, 2020.

Yan, K., Di Baldassarre, G., Solomatine, D. P., and Schumann, G. J. P.: A review of low-cost space-borne data for flood modeling: topography, flood extent and water level, Hydrol. Process., 29, 3368-3387, https://doi.org/10.1002/hyp.10449, 2015.

Zhao, C. S., Zhang, C. B., Yang, S. T., Liu, C. M., Xiang, H., Sun, Y., Yang, Z. Y., Zhang, Y., Yu, X. Y., Shao, N. F., and Yu, Q.: Calculating e-flow using UAV and ground monitoring, J. Hydrol., 552, 351-365, https://doi.org/10.1016/j.jhydrol.2017.06.047, 2017.

Table 1 Flood inundation points in Xuanhan City

Inundation Point	Discharge flow of the Jiangkou Reservoir	Location of inundation point	Inundation Point	Discharge flow of the Jiangkou Reservoir	Location of inundation point
A	12700m^3/s	The gate of the Local Tax Bureau	D	9800m^3/s	The Wangjia square
B	12000m^3/s	The entrance of China Construction Bank	E	7000m^3/s	Riverwalk outside the Lower Town Street
C	11200m^3/s	The gate of Red Army Memorial Park	F	6000m^3/s	Riverwalk outside the Westside Police Station

Table 2 List of computer hardware

Computer hardware	Hardware specifications
Central Processing Unit(CPU)	12th Gen Intel(R) Core(TM) i9-12900K 3.20 GHz
Graphics Processing Unit(GPU)	NVIDIA GeForce RTX 3090 Ti
Random Access Memory(RAM)	64GB
Solid State Drive(SSD)	1TB

Tabel 3 HEC-RAS model settings

HEC-RAS settings	Value
Initial Manning's coefficient	0.04（river channel） 0.06（floodplain and riverbank）
Initial river channel slope (downstream boundary condition)	0.00084 m/m
Time step for the flood hydrograph (upstream boundary condition)	1 hour
computational mesh size	5m x 5m
Computation and Output interval	2 minutes

Table 4 The computational time for floodplain mapping and the storage size of the inundation raster map

Terrain data resolution	Floodplain mapping time	Computing time for a single inundation raster map	Average storage size of a single inundation raster map
30m	6 m	0.38s	9KB
15m	9 m	0.56s	16KB
10m	10 m	0.66s	43KB
5m	12 m	0.78s	49KB
1m	1 h:36 m	6s	886KB
6cm	18 h:24 m	69s	364416KB

Table 5 Description of topographic variables used as independent explanatory variables for modeling. Descriptions are based on Salekin et al., (2021), Harris and Baird (2019), and the SAGA-GIS Tool Library Documentation (v8.5.1).

Topographic variables	Description	Formula/Units
Elevation	Elevation above sea level in meters.Elevation is a critical topographic parameter affecting water flow speed, direction, and energy.	Meters
Topographic Position Index	Difference between elevation of the cell and the mean of the elevation in surrounding cells, calculated by dividing the elevation difference by its standard deviation. It helps determine areas where water collects or disperses, influencing flow paths and ponding locations.	No unit Value > 0 when the cell is higher than its surroundings,zero when in a flat area or mid-slope and < 0 when lower than its surroundings.
Terrain ruggedness index	A measure of terrain complexity/ heterogeneity. It calculates the sum change in elevation between a grid cell and its neighbouring grid cells. Rugged terrain can increase flow friction, affecting both flow velocity and water kinetic energy.	Meters Value is always ≥0 m, where 0 represents the minimum roughness
Wind Exposition Index	Calculates the average wind effect across all directions using an angular step. This index indirectly reflects the impact of topography on flow paths by evaluating the terrain's openness or shielding characteristics.	No unit Value < 1 indicates wind-shadowed areas, value > 1 indicates areas exposed to wind.
Morphometric Protection Index	Analyses the immediate surrounding of each cell up to a given distance and evaluates how the relief protects it. This index helps assess the influence of terrain on flow paths.	No unit Value > 0 when the cell is protected and < 0 when it is not.
Vector ruggedness measure	A measure of terrain complexity/variance that captures variability in slope and aspect in a single measure. This index assists in identifying areas where water flow might be obstructed.	No unit Natural terrain has values between 0 and 0.4

Table 6 modeling results of inundation boundary line and flood depth produced using different resolution DTMs at six inundation points

Inundation point	Discharge（m^3/s）	Simulation results at different DTM resolution					
		0.06m	1m	5m	10m	15m	30m
A	12700	0	-0.09m	8.3m	9.8m	12.2m	16.8m
B	12000	0	0.06m	0.07m	4.5m	14.0m	14.0m
C	11200	0	0.05m	0.10m	0.71m	87m	34m
D	9800	0	0.03m	-0.02m	0.19m	5.1m	37.1m
E	7000	0	0.01m	0.02m	0.17m	11.5m	25.7m
F	6000	0	-0.03m	0.03m	0.50m	1.10m	8.0m

Note: The green colour indicates that the simulated inundation boundary is in coincidence with the benchmark boundary , and the numbers inside indicate the average error between the simulated inundation boundary's flood depth and the benchmark; the red colour indicates that the simulated inundation boundary is not in coincidence, and the numbers inside indicate the average distance that the simulated inundation boundary differs from the benchmark.

Table 7 Summary of the topographic attributes index for the standard（6cm DTM）

Topographic attribute index	6cm DTM			
	Min	Max	Mean	SD
Elevation	262.29	355.70	290.64	16.23
TPI	-2.87	28.51	0.04	1.05
TRI	0.00	38.28	0.13	1.45
WEI	1.26	0.79	1.01	0.10
MPI	0.00	1.52	0.31	0.31
VRM	0.00	0.70	0.03	0.09

Table 8 MAE of six topographic attribute metrics at different resolutions

topographic attribute index	MAE results at different DTMresolution				
	1m	5m	10m	15m	30m
Elevation	0.404	1.403	**1.617**	5.438	8.255
TPI	1.024	**3.412**	5.485	6.957	9.734
TRI	1.437	**5.014**	8.024	10.140	14.102
WEI	0.034	0.075	**0.083**	0.105	0.121
MPI	0.148	0.253	**0.259**	0.321	0.312
VRM	0.070	0.100	**0.109**	0.143	0.115

Note: Bold black values indicate abrupt/step changes before and after the value.

Fig.1

Location of study area, Xuanhan City, China, and the flood core control area (yellow boundary line) shown on the satellite map (from © Google Earth) and the orthophoto, including drone survey area, flood modeling area and six inundation points

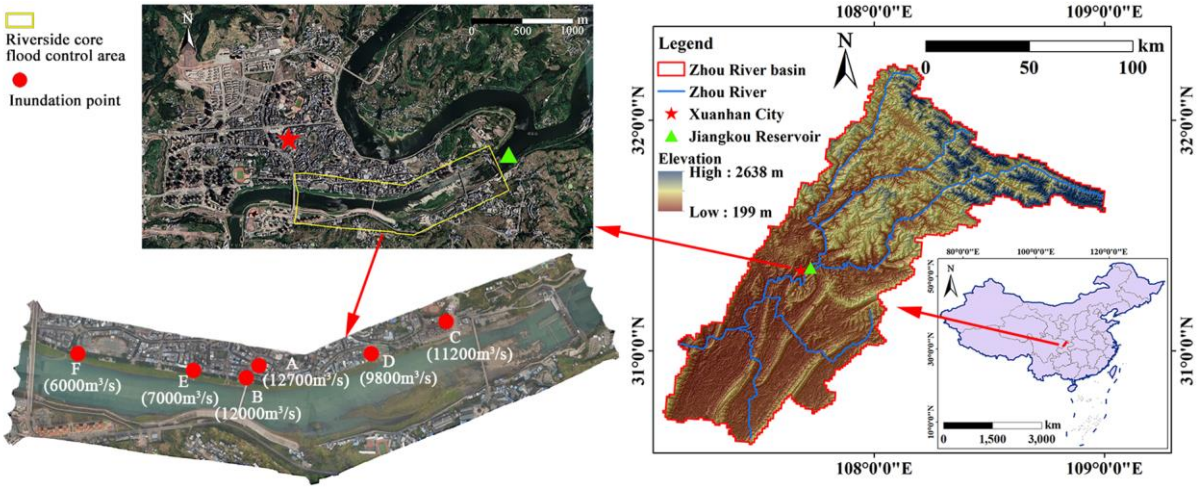

Fig.2

Flowchart of drone images acquisition and processing

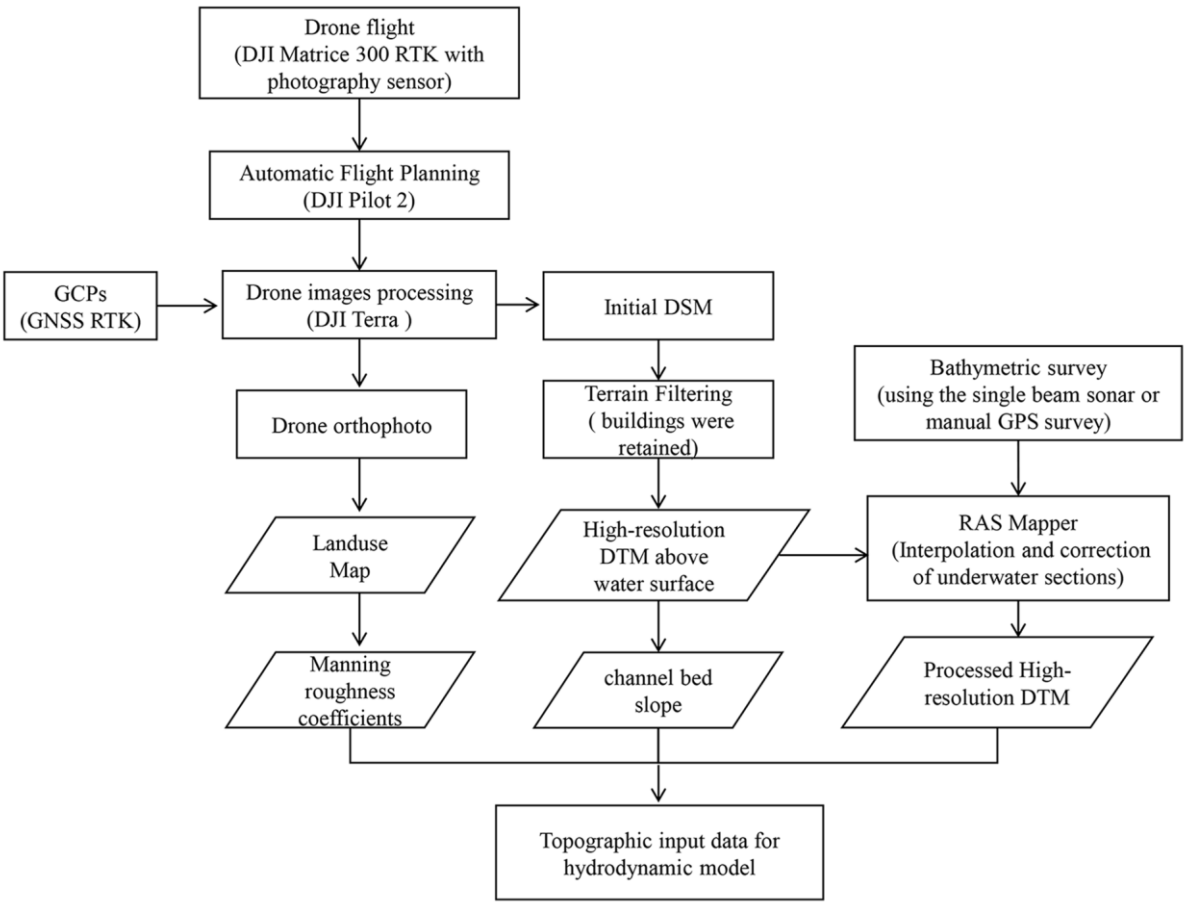

Fig.3

Visualization of DTM generation from DSM using PCI Geomatica: (a) DSM, (b) DTM, (c) Orthophoto.

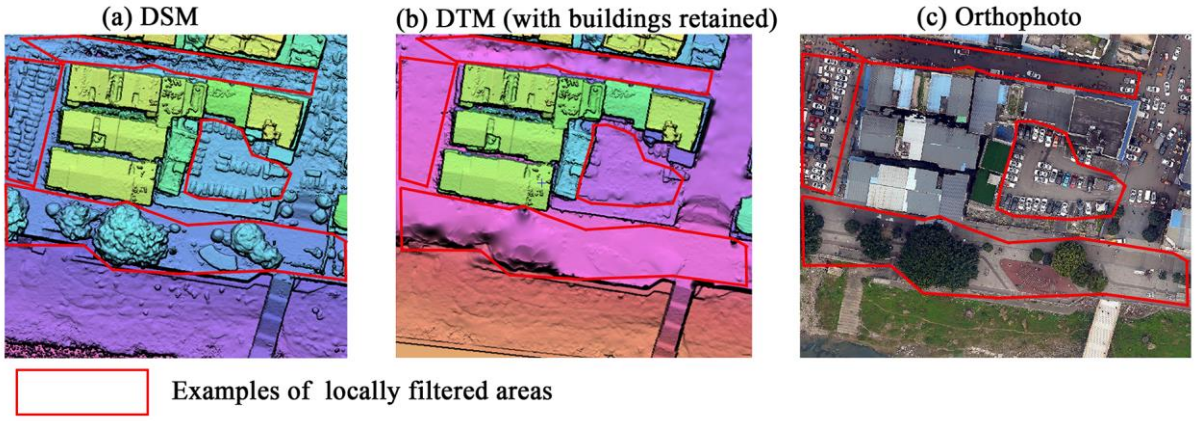

Fig.4

Generalization of the underwater cross-section

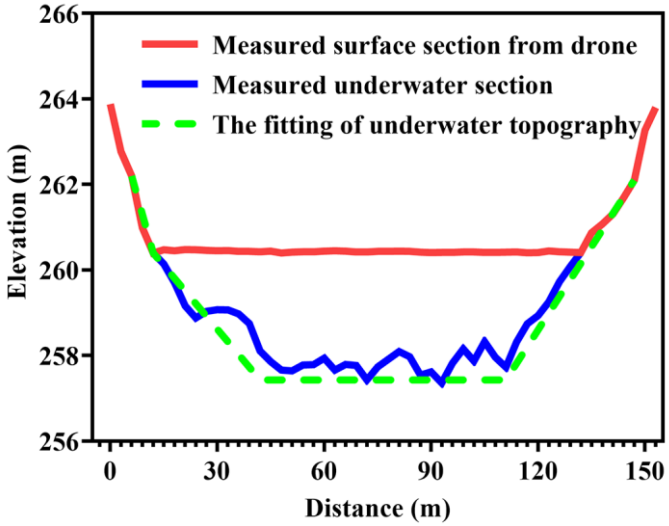

Fig.5

Mesh used for all simulations with 6 cm DTM in the HEC-RAS and hydrograph of the typical flood event

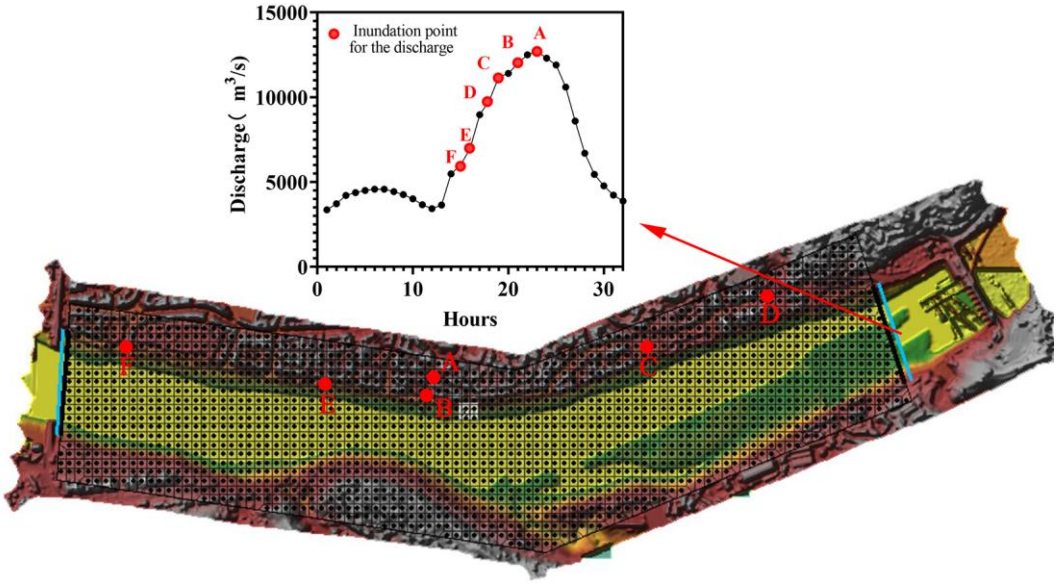

Fig.6

Comparison and validation of inundation point simulation results with historical flood boundary lines (The inner six images are on-site survey images about six inundation points and the outer six localized magnified orthophotos are the corresponding flood mapping results from HEC-RAS)

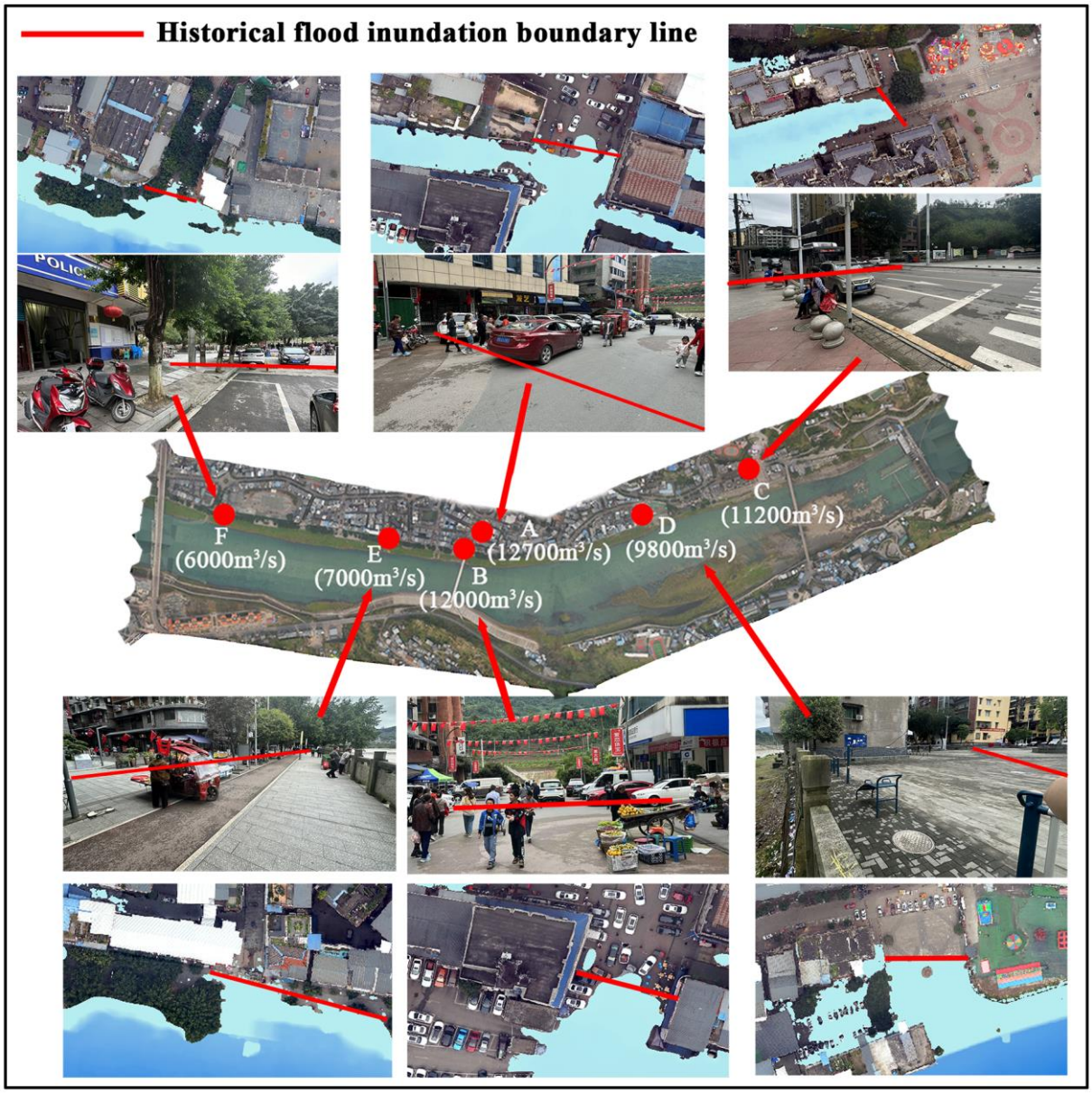

Fig. 7

The flood simulation results for the maximum flood peak flow based on the 6 cm DTM: (a) inundation area, (b) inundation depth.

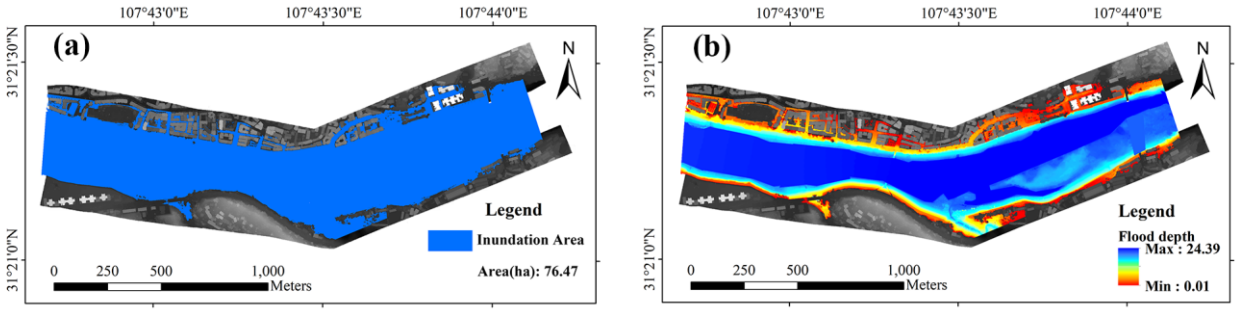

Fig. 8

Spatial and statistical analyses of the effects of DTM resolution on the simulated inundation Extent and flood depth by comparing the benchmark conditions(6cm DTM)

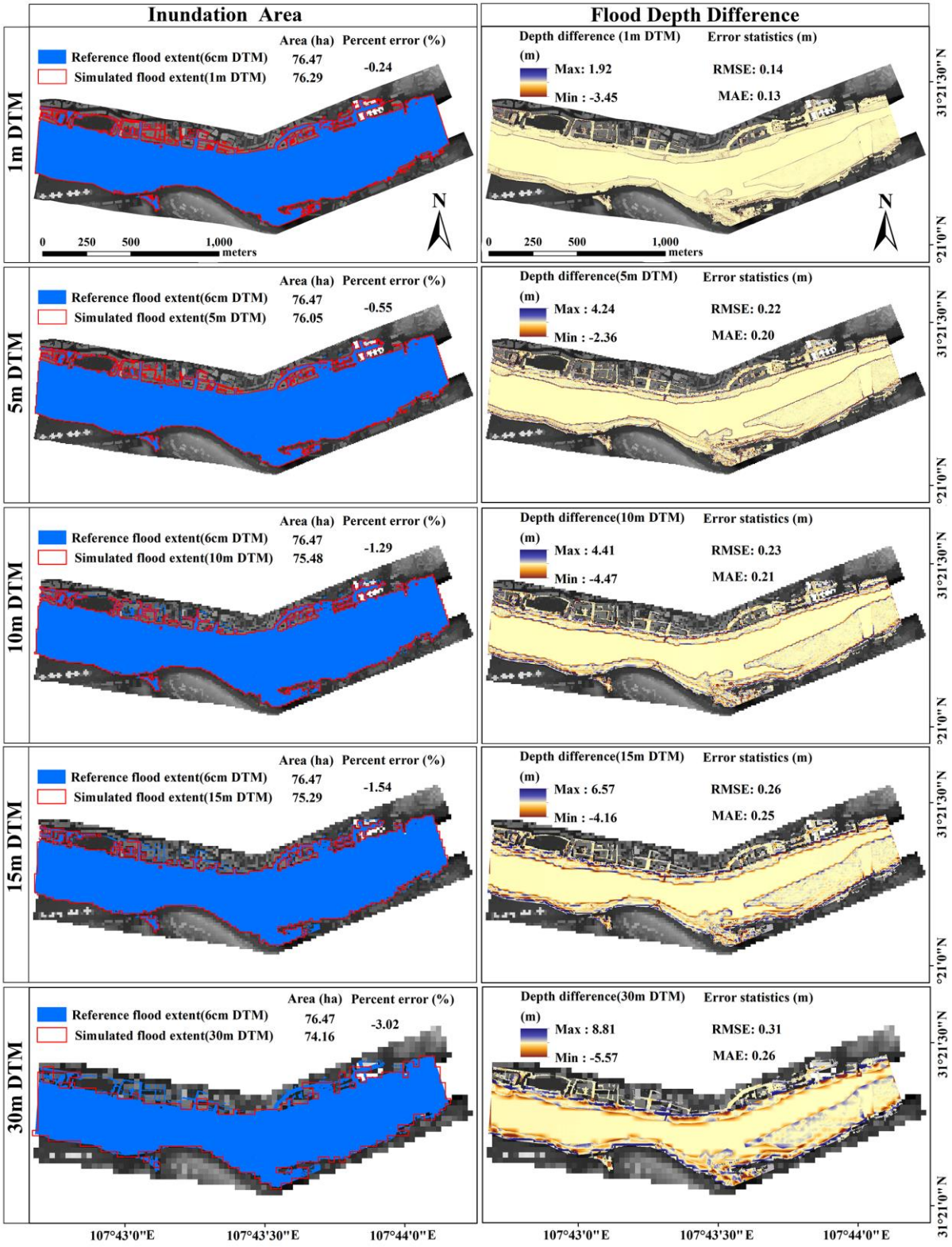

Fig. 9

Trend of the inundation area and mean flood depth derived from DTMs with different resolution at the flood peak (a) main river channel, (b) floodplain and riverbank (out of main river channel)

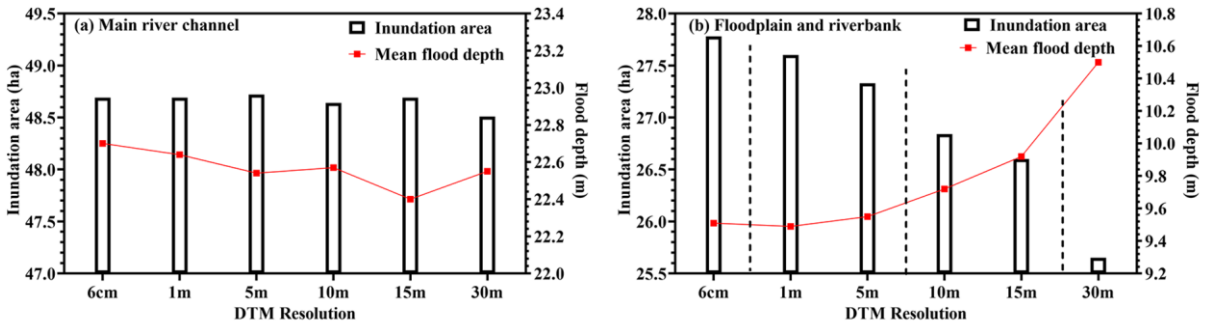

Fig. 10

Inundation modeling results at point C(11200m^3/s) produced using different resolution DTMs

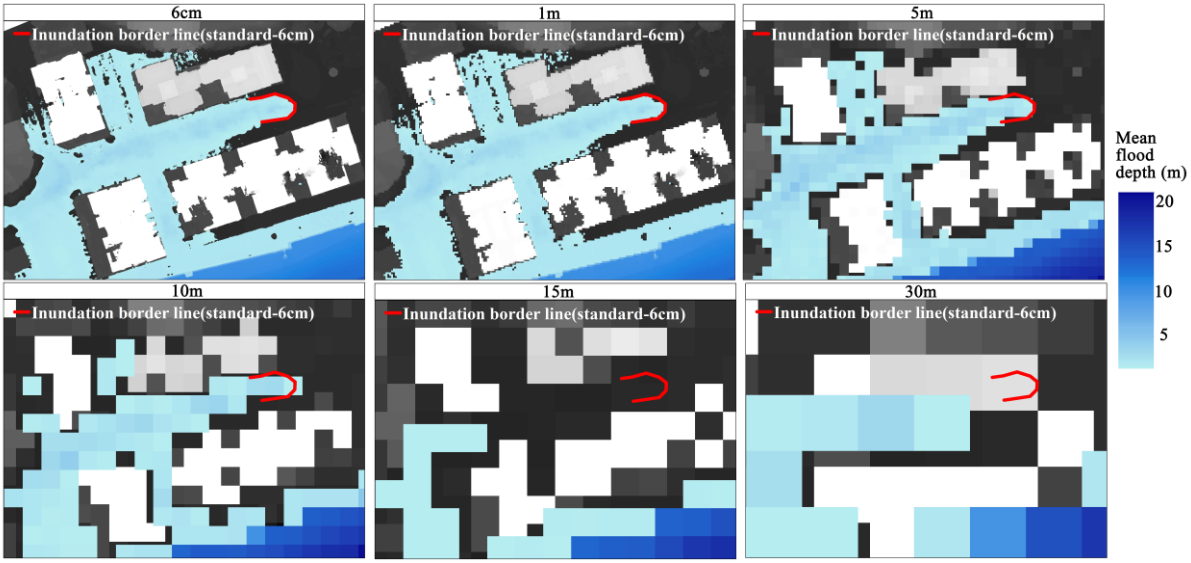

Fig. 11

Variations in absolute errors for topographic features derived at different resolutions of DTMs

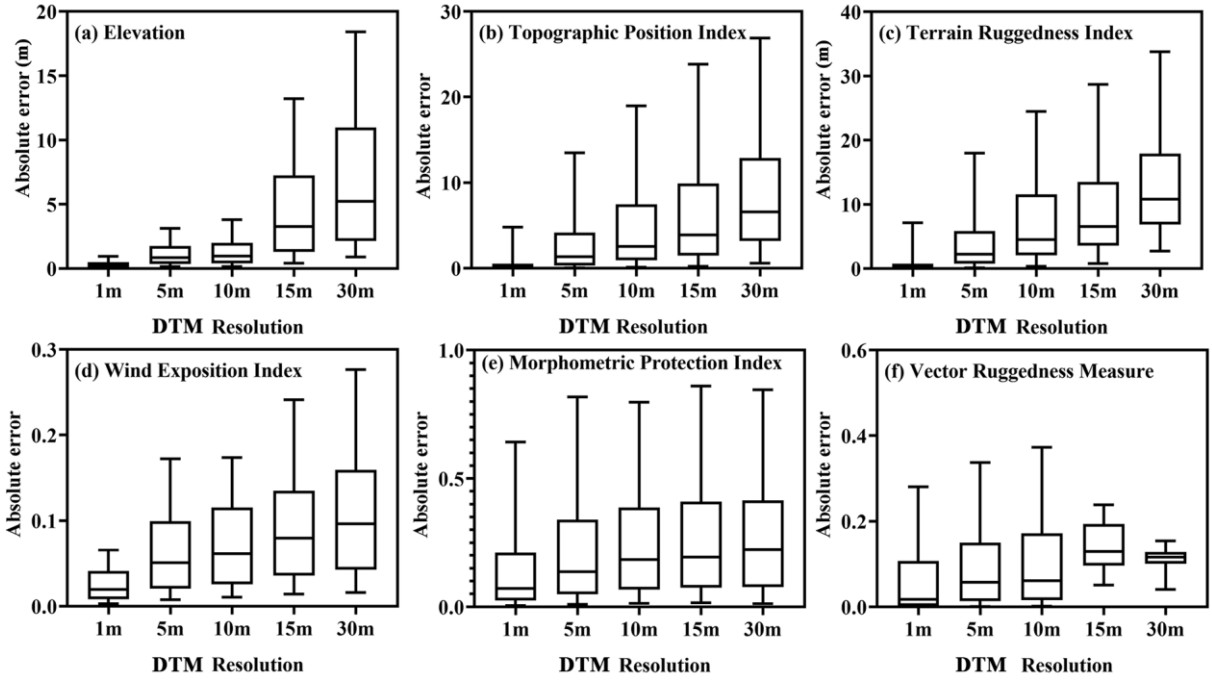

figure captions

Fig.1 Location of study area, Xuanhan City, China, and the flood core control area (yellow boundary line) shown on the satellite map (from © Google Earth) and the orthophoto, including drone survey area, flood modeling area and six inundation points

Fig. 2 Flowchart of drone images acquisition and processing

Fig. 3 Visualization of DTM generation from DSM using PCI Geomatica: (a) DSM, (b) DTM, (c) Orthophoto.

Fig. 4 Generalization of the underwater cross-section

Fig. 5 Mesh used for all simulations with 6 cm DTM in the HEC-RAS and hydrograph of the typical flood event

Fig. 6 Comparison and validation of inundation point simulation results with historical flood boundary lines (The inner six images are on-site survey images about six inundation points and the outer six localized magnified orthophotos are the corresponding flood mapping results from HEC-RAS)

Fig. 7 The flood simulation results for the maximum flood peak flow based on the 6 cm DTM: (a) inundation area, (b) inundation depth.

Fig. 8 Spatial and statistical analyses of the effects of DTM resolution on the simulated inundation Extent and flood depth by comparing the benchmark conditions(6cm DTM)

Fig. 9 Trend of the inundation area and mean flood depth derived from DTMs with different resolution at the flood peak (a) main river channel, (b) floodplain and riverbank (out of main river channel)

Fig. 10 Inundation modeling results at point C(11200m^3/s) produced using different resolution DTMs

Fig. 11 Variations in absolute errors for topographic features derived at different resolutions of DTMs